Journal of Power Sources 241 (2013) 440–448

Contents lists available at SciVerse ScienceDirect

Journal of Power Sources

journal homepage: www.elsevier.com/locate/jpowsour

Fabrication and characterization of all-ceramic solid oxide fuel cells based on composite oxide anode

Jeonghee Kim [a,b], Dongwook Shin [c], Ji-Won Son [a], Jong-Ho Lee [a], Byung-Kook Kim [a], Hae-June Je [a], Hae-Weon Lee [a], Kyung Joong Yoon [a,*]

[a] High-Temperature Energy Materials Research Center, Korea Institute of Science and Technology, Hwarangno 14-gil 5, Seongbuk-gu, Seoul 136-791, Republic of Korea
[b] Department of Fuel Cells and Hydrogen Technology, Hanyang University, Seoul, Republic of Korea
[c] Division of Materials Science and Engineering, Hanyang University, Seoul, Republic of Korea

HIGHLIGHTS

- High performance all-ceramic anode is fabricated and electrochemically evaluated.
- Impedance characteristics are analyzed using half cell measurements.
- Rate limiting processes for individual electrodes are clarified.
- Chemical capacitance causes the major impedance for ceramic anode.

ARTICLE INFO

Article history:
Received 12 March 2013
Received in revised form
16 April 2013
Accepted 27 April 2013
Available online 9 May 2013

Keywords:
Solid oxide fuel cells
Ceramic anode
Impedance spectroscopy
Chemical capacitance
Rate limiting process

ABSTRACT

All-ceramic solid oxide fuel cells (SOFCs), which offer advantages in carbon tolerance, sulfur resistance and redox stability, are fabricated and evaluated. The electrolyte-supported cells are composed of a $La_{0.75}Sr_{0.25}Cr_{0.5}Mn_{0.5}O_{3-\delta}$ (LSCM)–$Ce_{0.9}Gd_{0.1}O_{1.95-\delta}$ (GDC) anode, an Y_2O_3-stabilized ZrO_2 (YSZ) electrolyte, a GDC interdiffusion barrier layer, and a $La_{0.8}Sr_{0.2}Co_{0.2}Fe_{0.8}O_{3-\delta}$ (LSCF)–GDC cathode. A particle-dispersed glycine-nitrate process is developed to synthesize extremely fine and homogeneous LSCM–GDC ceramic composite powders. The electrochemical performance of the LSCM–GDC anode is comparable to that of conventional Ni-based anodes. The impedance spectra of the all-ceramic SOFCs are successfully interpreted by the independent characterization of the individual electrodes via half-cell measurements. The impedance of the LSCM–GDC anode is dominated by a low-frequency arc originating from the "chemical capacitance", which is associated with the variation of the oxygen non-stoichiometry in the mixed conducting ceramic electrode. In addition, the impedance arc associated with the electrode–gas interaction is observed in the LSCM–GDC anode. The rate-limiting processes for the LSCF–GDC cathode are observed to be solid-state oxygen diffusion and surface chemical exchange. Herein, the reaction mechanisms and rate-limiting processes of the all-ceramic SOFCs are discussed in detail and compared with those of conventional Ni-based SOFCs.

1. Introduction

The solid oxide fuel cell (SOFC) is a solid-state device that directly converts the chemical energy of gaseous fuel to electricity through electrochemical reactions and offers numerous advantages over conventional power generation systems, such as high efficiency, low environmental impact, multi-fuel capability, and modularity [1–5]. Recently, SOFCs with all-ceramic anodes have become an exciting research area because they possess attractive features such as reduction–oxidation (redox) stability, coking resistance, and sulfur tolerance [6–9]. The metallic components of the anode such as Ni induces performance degradation and catastrophic failure during redox cycles, which may result from seal leakage, the interruption of the fuel supply, or system shut down due to large and irreversible volume changes accompanied by metal-oxide transitions [10–16]. In addition, Ni promotes coke deposition in the presence of

* Corresponding author. Tel.: +82 2 958 5515; fax: +82 2 958 5529.
E-mail addresses: kjyoon@kist.re.kr, kyungjoong.yoon@gmail.com (K.J. Yoon).

0378-7753/$ – see front matter © 2013 Elsevier B.V. All rights reserved.
http://dx.doi.org/10.1016/j.jpowsour.2013.04.139

hydrocarbons, especially when the steam-to-carbon ratio is low, and is readily poisoned by trace amounts of sulfur [17–24]. Therefore, it is highly desirable to develop an alternative ceramic-based anode material with improved redox, coking, and sulfur tolerance, which would substantially simplify the SOFC systems operating on fuels derived from natural gas, coal and biomass and hence reduce SOFC packaging and costs. The ideal solution would be a single phase mixed conducting ceramic electrode in which the entire electrode surface would be active for electrochemical reaction [25]. However, in practice, it is extremely difficult to develop a single phase oxide material that fulfills the rigorous requirements for anodes, such as high electronic conductivity, ionic conductivity, chemical stability, mechanical strength, thermal expansion match, chemical compatibility, etc. [26]; thus, the need for a composite approach has been stressed [27,28]. Although some composite anodes have exhibited acceptable properties, their electrochemical performance has been substantially lower than that of the conventional Ni-based anode in most cases. To improve the performance of all-ceramic SOFCs, it is essential to understand the reaction mechanisms and rate-limiting processes involved because detailed knowledge of the pertinent electrode reactions allows for the identification of current limitations and the determination of future research directions.

In this work, all-ceramic SOFCs were fabricated and electrochemically evaluated. The electrolyte-supported cells were composed of a $La_{0.75}Sr_{0.25}Cr_{0.5}Mn_{0.5}O_{3-\delta}$ (LSCM)–$Ce_{0.9}Gd_{0.1}O_{1.95-\delta}$ (GDC) anode, an Y_2O_3-stabilized ZrO_2 (YSZ) electrolyte, a GDC interdiffusion barrier layer, and a $La_{0.8}Sr_{0.2}Co_{0.2}Fe_{0.8}O_{3-\delta}$ (LSCF)–GDC cathode. The performance of the all-ceramic SOFC was compared with that of the conventional Ni-based SOFC, and a comprehensive understanding of the electrode reaction kinetics was obtained by the independent characterization of the individual electrodes.

2. Experimental

A composite LSCM–GDC powder was prepared by the particle-dispersed glycine-nitrate process [29]. Commercially purchased GDC powder was dispersed in distilled water using a dispersant. The nitrate precursors of lanthanum, strontium, chromium, and manganese were added to the mixture and mixed according to the targeted stoichiometry with glycine. The glycine/nitrate/powder mixture was combusted, and the raw powder was calcined at 1200 °C in air for 2 h. After calcination, the phase purity was verified by X-ray diffraction (XRD) analysis, and the particle morphology was examined using transmission electron microscopy (TEM).

Electrolyte-supported button cells were fabricated using ~300 μm-thick 8 mol % YSZ substrates. Pastes were prepared by mixing the powders with desired amounts of solvent, dispersant, binder, and plasticizer. An LSCM–GDC anode with the active area of 1 cm^2 was screen printed on one side of the electrolyte substrate, and a GDC interdiffusion barrier layer was screen printed on the other side, followed by sintering at 1200 °C for 2 h in air. Then, an LSCF–GDC cathode was screen printed over the GDC interdiffusion barrier layer, and cell fabrication was completed by firing the cathode at 1050 °C in air for 2 h. The fabricated cells were tested at 750–850 °C with humidified hydrogen (97% H_2–3% H_2O) as the fuel and air as the oxidant using a ceramic-glass composite sealant and an Inconel-based interconnect. Electrochemical measurements were performed using a Solartron 1260/1287 potentiostat and a frequency response analyzer. After testing, the cross sections of the cells were examined by scanning electron microscopy (SEM), and the microstructural features were investigated using the image analysis software program ImageJ.

Anode symmetrical half cells were fabricated using 2–3 mm-thick YSZ discs as the electrolyte substrates. Anode paste was screen printed onto both sides of the discs and fired at 1200 °C in air for 2 h. To fabricate cathode half cells, a GDC interdiffusion barrier layer was screen printed on both sides of the 2–3 mm-thick YSZ discs and fired at 1200 °C in air for 2 h. Then, an LSCF–GDC cathode was screen printed on GDC, and the entire structure was fired at 1050 °C in air for 2 h. The fabricated half cells were tested in a quartz tube reactor at 750–850 °C under various gas compositions, and the obtained impedance spectra were analyzed by fitting to an equivalent circuit model using the Z-view 3.1C software program.

3. Results and discussion

LSCM–GDC composite powder was synthesized using the novel powder-dispersed glycine-nitrate method. The glycine-nitrate method is a self-sustaining combustion technique for synthesizing high-quality ceramic powders from aqueous solution of metal nitrate and glycine [29]. Because the glycine-nitrate method produces excellent powder properties for various ceramic processing applications, it has been widely used in many areas through diverse modifications [30,31]. In particular, the synthesis of yttrium chromite-ceria composite powder through the single step combustion of the glycine-nitrate process has been reported for SOFC ceramic anode applications [32]. In the present work, nano-scale LSCM–GDC composite powder was synthesized by the powder-dispersed glycine-nitrate method. In this process, commercially purchased GDC powder was dispersed in a solution of glycine and nitrate precursors of LSCM, and the LSCM–GDC composite powder was formed *in-situ* through self-combustion. Fig. 1 shows a TEM image of the composite powder synthesized by particle-dispersed glycine-nitrate process after calcination at 1200 °C in air. The surface of GDC inclusion particles were coated with extremely fine LSCM particles, which were formed from the nitrate precursors through combustion. The particle size of the GDC powder was 200–300 nm, while that of the LSCM primary powder was 20–30 nm. Such a composite powder is expected to provide excellent phase connectivity, homogeneity, thermo-mechanical strength, and triple phase boundary length in the form of a porous electrode.

In-situ phase analysis was performed from room temperature to 1200 °C using high-temperature XRD, the results of which are shown in Fig. 2(a). All of the peaks were indexed to the LSCM orthorhombic perovskite structure and GDC cubic fluorite structure, and no indication of secondary phase formation or major peak shift was detected within the sensitivity of the instrument. Fig. 2(b) compares the aforementioned XRD patterns with those of the LSCM–GDC composite powder measured at 25 °C after calcination at 1200 °C in air and after exposure to a reducing atmosphere ($pO_2 = 4 \times 10^{-23}$ MPa) at 800 °C for 12 h. No decomposition product was detected after reduction. Therefore, LSCM–GDC was confirmed to be chemically stable under both the processing and operating conditions of the SOFC anode.

To evaluate the electrochemical performance of the ceramic anode, the electrolyte-supported SOFC employing an LSCM–GDC anode was fabricated. The cell was composed of a ~15 μm-thick LSCM–GDC anode, ~300 μm-thick YSZ electrolyte, ~10 μm-thick GDC barrier layer, and ~15 μm-thick LSCF–GDC cathode. A GDC interdiffusion barrier layer was placed between the YSZ electrolyte and LSCF–GDC cathode to prevent unfavorable solid-state reactions [33–35]. The microstructure of the LSCM–GDC anode is illustrated in Fig. 3. The cross-sectional image in Fig. 3(a) reveals a highly porous structure with a uniform thickness of ~15 μm. The porosity of the anode was measured to be ~30% by image analysis. The SEM image in Fig. 3(b), obtained in the BSE mode, shows the particle size distribution of the composite powder. The LSCM

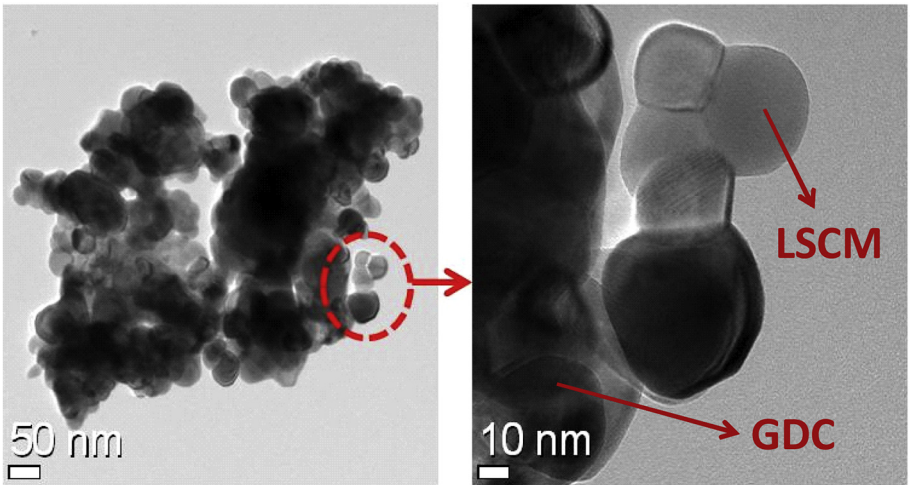

Fig. 1. TEM image of LSCM–GDC composite powder synthesized by particle-dispersed glycine-nitrate method.

powder was gray, and the GDC powder was white based on energy-dispersive X-ray spectroscopy (EDX) analysis. The results confirm that the powders exhibited homogeneous structures with well-connected fine particles after sintering.

Fig. 4 shows the electrochemical performance of the all-ceramic SOFC. A conventional cell employing a Ni–YSZ anode was also fabricated and tested as a reference. The cell structure and component materials of the all-ceramic cell and the reference cell were identical except for the anode. Fig. 4 compares the current density-voltage (I–V) characteristics and corresponding power

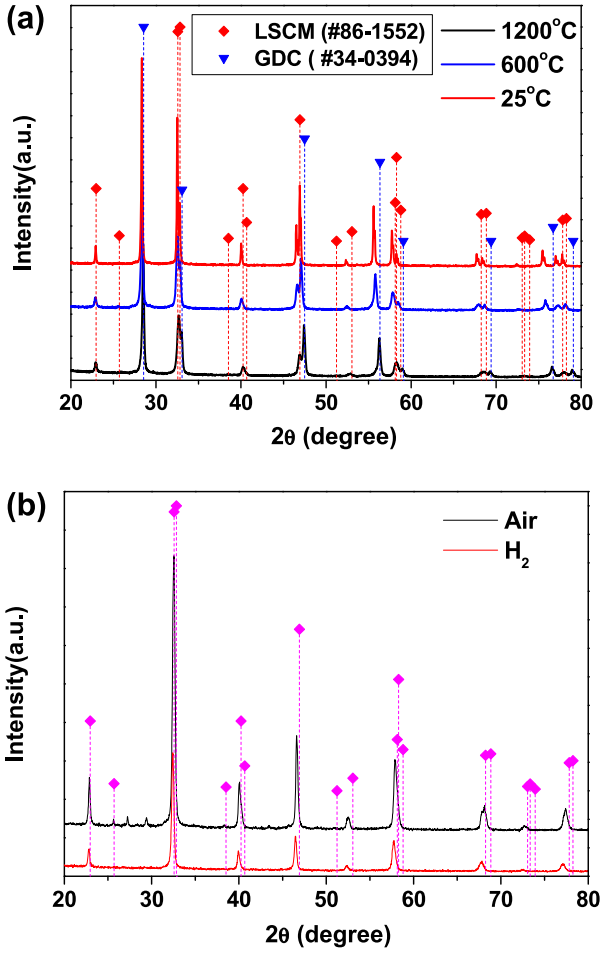

Fig. 2. (a) High temperature XRD patterns of LSCM–GDC composite powder measured between room temperature and 1200 °C, and (b) XRD patterns collected at 25 °C after calcinations in air and after reduction in hydrogen at 800 °C for 12 h.

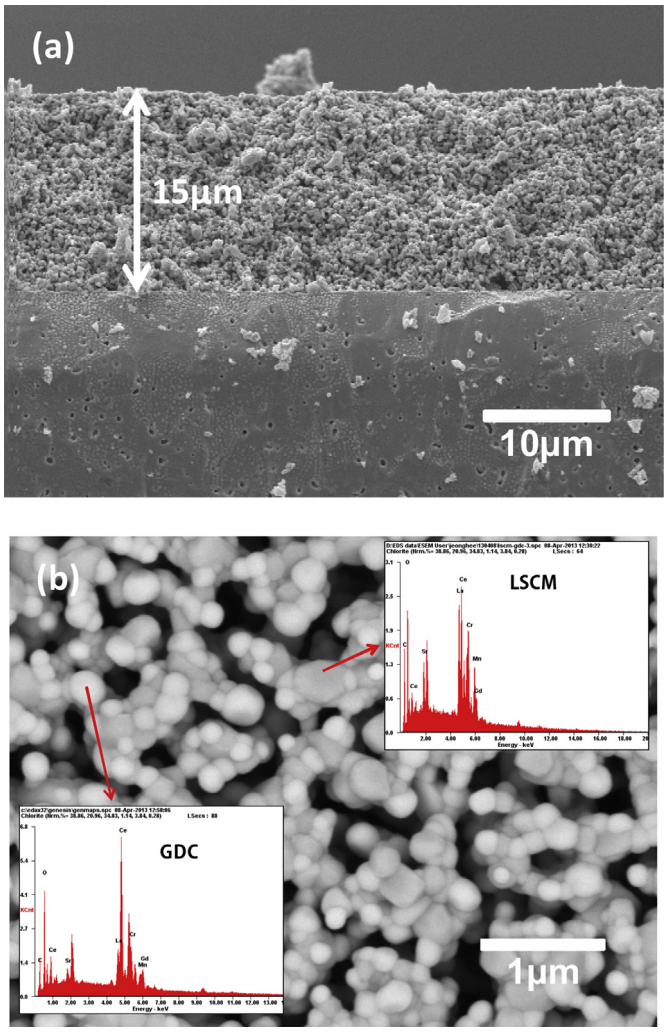

Fig. 3. SEM image of the LSCM–GDC anode: (a) SE image of the fractured cell, and (b) BSE image and EDX results of the LSCM–GDC composite structure. The LSCM is gray, and the GDC is white.

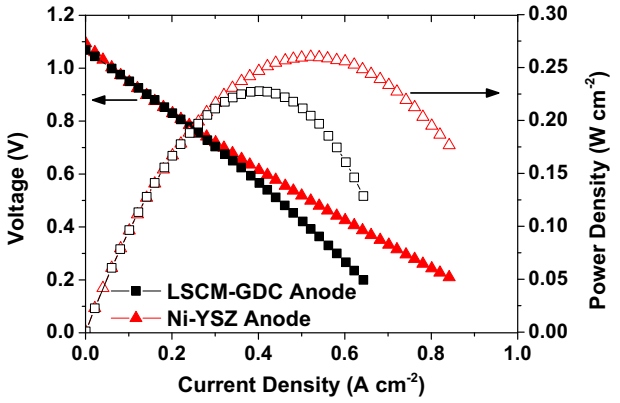

Fig. 4. *I–V* curves of the electrolyte-supported cells with LSCM–GDC and Ni–YSZ anodes measured at 800 °C with humidified hydrogen (97% H_2 + 3% H_2O) as fuel and air as oxidant.

densities of the two cells measured at 800 °C with humidified hydrogen (97% H_2 + 3% H_2O) as the fuel and air as the oxidant. Table 1 summarizes the performance of the two cells. The cell with a Ni–YSZ anode showed slightly higher power output than the all-ceramic cell, but the performance of the two cells was comparable. The performance of the electrolyte-supported cell is dominated by the ohmic resistance of the electrolyte, and the information obtained from the *I–V* curves in Fig. 4 only represents the overall performance of the conventional electrolyte-supported cell employing the LSCM–GDC anode. A comprehensive understanding on the performance of the electrode could be obtained from the impedance spectra, in which the contribution of the ohmic resistance of the electrolyte could be distinguished. Fig. 5 shows the impedance spectra of the two cells measured at 800 °C with humidified hydrogen (97% H_2 + 3% H_2O) as the fuel and air as the oxidant under open-circuit conditions. In the Nyquist plot (Fig. 5(a)), the high-frequency intercept on the real axis corresponds to the ohmic resistance of the cell, and the polarization resistance can be obtained by subtracting the high-frequency intercept from the low-frequency intercept [36]. The cell resistance values obtained from the impedance spectra are summarized in Table 2. The all-ceramic cell showed slightly higher ohmic resistance than that with the Ni–YSZ anode because LSCM is a *p*-type ceramic conductor and exhibits lower electronic conductivity than Ni, especially in a reducing atmosphere [37]. The polarization resistance of the reference cell was also slightly lower, which implies that the catalytic activity of the Ni–YSZ anode was somewhat higher than that of the LSCM–GDC anode. In general, the electrode resistance of the ceramic anode is known to be larger than that of the Ni–YSZ cermet by at least one order of magnitude due to its inferior catalytic activity and electronic conductivity [38]. However, based on Tables 1 and 2, the performance of the LSCM–GDC anode is comparable to that of the Ni–YSZ cermet, possibly due to the excellent microstructure of the composite electrode resulting from the particle-dispersed glycine-nitrate process. Thus, it is suggested that the merits of the ceramic anode such as carbon, sulfur, and

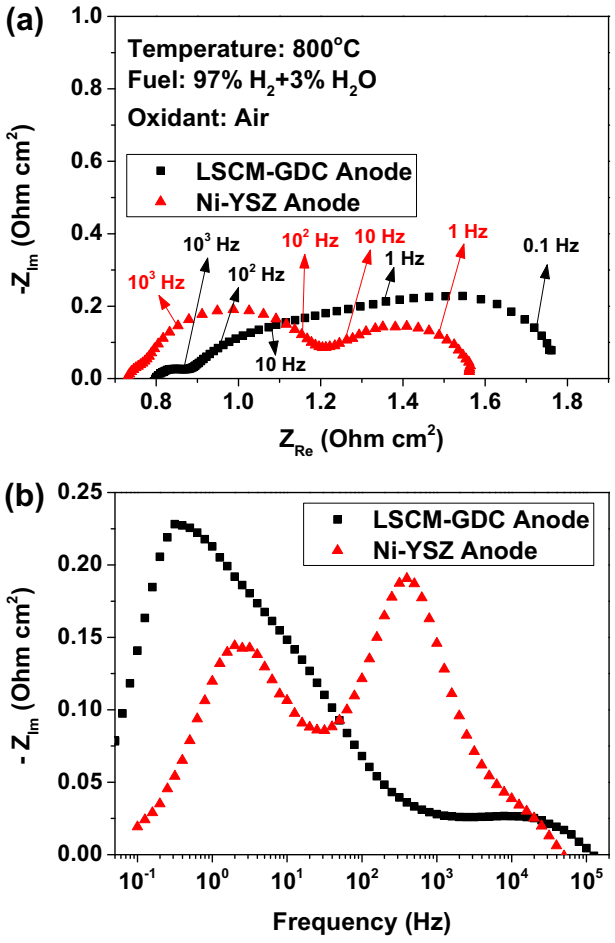

Fig. 5. Impedance spectra obtained from the electrolyte-supported cells with LSCM–GDC and Ni–YSZ anodes measured at 800 °C with humidified hydrogen (97% H_2 + 3% H_2O) as fuel and air as oxidant; (a) Nyquist plot and (b) Bode plot of the imaginary part.

redox tolerance could be effectively utilized in practical applications by employing the synthesis technique presented in this paper. The Bode plot of the imaginary parts in Fig. 5(b) shows the frequency response of the impedance of the two cells. Although the performances and cell resistances of the two cells were comparable, it is clearly observed that the major peaks of the impedance spectra are entirely different. For the all-ceramic cell, the major peak was observed in the low-frequency region below 1 Hz, with small embedded peaks at 10–10^2 Hz, whereas the reference cell showed two clearly separated peaks with characteristic frequencies of ~10^3 Hz and ~10 Hz. The large difference in the peak frequencies of the two cells implies that the major relaxation processes of the LSCM–GDC ceramic anode are different from those of the Ni–YSZ cermet anode. To further improve the performance of the ceramic anode, it is necessary to clarify the sluggish elementary kinetic processes observed in the impedance spectra and focus on

Table 1
The power densities at 0.7 V and maximum power densities of the electrolyte-supported cells with LSCM–GDC anode and Ni–YSZ anode, measured at 800 °C with humidified hydrogen (97% H_2 + 3% H_2O) as fuel and air as oxidant.

	LSCM–GDC anode	Ni–YSZ anode
Power density at 0.7 V (W cm^{-2})	0.21	0.22
Maximum power density (W cm^{-2})	0.23	0.26

Table 2
The Ohmic and polarization resistances of the electrolyte-supported cells with LSCM–GDC anode and Ni–YSZ anode obtained from the impedance spectra measured at 800 °C with humidified hydrogen (97% H_2 + 3% H_2O) as fuel and air as oxidant.

	LSCM–GDC anode	Ni–YSZ anode
Ohmic resistance (Ω cm^2)	0.80	0.76
Polarization resistance (Ω cm^2)	0.95	0.81

facilitating the rate-limiting reactions. In general, the impedance spectra of the full cell contain contributions from various physical and chemical processes, and it is difficult to deconvolute the spectra because of a number of overlapping semicircles originating from both the anode and cathode. Therefore, for a comprehensive understanding of the electrode kinetics, the impedance spectra associated with anodic and cathodic processes should be independently measured and analyzed.

The contributions of the anode and cathode processes can be separated using a reference electrode in full cell measurements [39]. However, it was reported that the utilization of a reference electrode in a solid-state ionic conductor is not as simple as in liquid-state electrochemical experiments because data collection is strongly influenced by the geometrical configuration, and inadequate positioning of the reference electrode as well as small misalignments in the relative position of the working and counter electrodes could induce significant errors [40,41]. An alternative method is the symmetric half-cell measurements. Half cells with the same electrodes on both sides of the electrolyte could provide useful information for the independent characterization of cathode and anode processes, especially when the electrochemical data of the full cell is too complex to interpret. To understand the full cell data in Fig. 5, the half cells of an LSCM–GDC anode, Ni–YSZ anode, and LSCF–GDC cathode were fabricated and electrochemically characterized. Fig. 6 shows the impedance spectrum and the equivalent circuit fitting results of the LSCM–GDC anode measured at 800 °C in humidified hydrogen (97% H_2 + 3% H_2O). The high-frequency intercept was normalized to the value of zero. Good fits were obtained using the equivalent circuit model, $L\ R_{Ohmic}\ (R_1\text{-}CPE_1)\ (R_2\text{-}CPE_2)$, according to the notation used elsewhere [42], indicating that the impedance spectrum is composed of two dominant arcs. The inductance, L, is attributed to the high-frequency artifacts arising from the apparatus. The ohmic resistance, R_{Ohmic}, includes the resistance of the electrolyte, the electrode, and the contact resistance associated with interfaces and current collection. Two standard resistor-constant phase element units ($R_1\text{-}CPE_1$ and $R_2\text{-}CPE_2$) correspond to the two arcs, and the constant phase element is expressed as $Z_{CPE} = (i\omega Q)^{-n}$, where ω is the cyclic frequency, Q the pseudo-capacitance, and n the exponent component. The Bode plot of the imaginary part of the impedance in Fig. 6(b) exhibits two dominant electrode processes with summit frequencies of 10–10^2 Hz and 0.1–1 Hz.

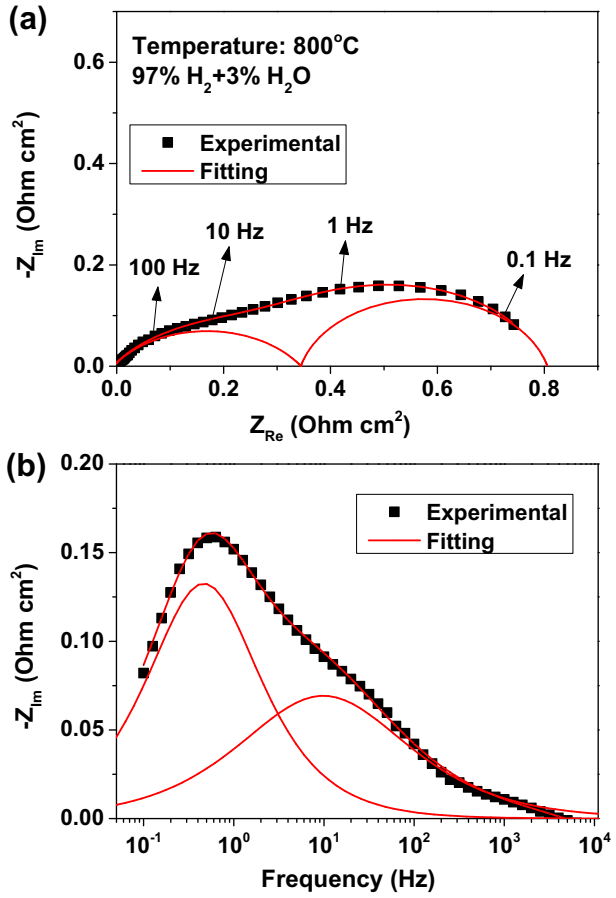

Fig. 6. Impedance spectrum of the LSCM–GDC half cell measured at 800 °C in humidified hydrogen (97% H_2 + 3% H_2O); (a) Nyquist plot and (b) Bode plot of the imaginary part. Solid lines represent equivalent circuit fitting results.

There are many elementary kinetic processes in SOFC anode reactions that can generate the impedance arcs: charge transfer between YSZ and Ni [43], diffusion of charged species to triple phase boundaries [44], adsorption of reactant species [45], desorption of product species [46], variation of oxygen concentration at the electrode/electrolyte interface [47], surface migration [48], gas diffusion [49], gas conversion [50], and variation of chemical species in the bulk of the electrode [51]. Although numerous studies have been reported to date [43,44,52–58], the elementary mechanism of the H_2–H_2O reaction on SOFC anodes is still controversial and has not been conclusively determined yet. In general, the high-frequency impedance with the characteristic frequency greater than 10^4 Hz is assigned to the electrode electrochemistry arising from the charge transfer reaction or electrical double layer at the two phase boundaries [43,44]. Because the high-frequency impedance is not clearly indicated in Fig. 6(b), it is suggested that the charge transfer reaction on the LSCM–GDC anode is sufficiently fast and that its contribution to the cell resistance is not significant. The mid-frequency impedance with the summit frequency of 10–10^4 Hz is commonly attributed to a gas–solid interaction (adsorption, dissociation, desorption, etc.) or surface diffusion of the adsorbed species [43,44,58,59]. At this stage, it is difficult to assign the specific processes among those to the mid-frequency arc observed in LSCM–GDC anodes. It is apparent that the contribution of the mid-frequency impedance is substantial, and its physical origin will be discussed later in this paper. A major peak was observed in the low-frequency range for the LSCM–GDC anode, as shown in Fig. 6(b). The low-frequency arc with a peak frequency below 1 Hz has been frequently observed for ceramic-based SOFC anodes [60–62], and its origin is controversial. Gas phase diffusion was suggested to be the dominant resistive process in the ceramic anode due to the low-frequency arc with the peak frequency of 0.2 Hz [60], but the relaxation frequency of the gas phase diffusion process is known to be 1–10 Hz, which does not match the low-frequency arc of the ceramic anode [63]. Furthermore, gas diffusion could be responsible for the major polarization loss in anodes supported by a thick anode substrate, but the contribution of gas diffusion is not expected to be significant in the electrolyte-supported design, which employs a thin and highly porous anode. The low-frequency arc associated with the SOFC anode could originate from gas conversion, which is caused by the local variation in the Nernst potential between the working and reference electrodes with the passage of current [50]. Gas conversion impedance is sensitive to test conditions such as gas flow rate, gas composition, temperature, and rig geometry and is usually observed in setups with a reference electrode outside the working chamber [50]. In this work, gas conversion impedance was not expected because the half-cell measurements were performed in a single-atmosphere setup in which the working and reference electrodes were placed in the same environment. In addition, as

will be mentioned later in this paper, a low-frequency arc was not observed from the Ni–YSZ anode half-cell measurements under the same test conditions. Therefore, gas conversion impedance may not be the proper explanation for the low-frequency impedance. The low-frequency arc, which was only observed in the ceramic anode, could be ascribed to the "chemical capacitance", which originates from the variation in the oxygen nonstoichiometry of the ceramic electrode. The chemical capacitance represents the capacity of the specimen to store chemical energy through oxygen vacancies upon changes in the local oxygen chemical potential. Electrochemical polarization leads to changes in the oxygen content of the ceramic electrode, and the chemical relaxation process associated with the variation in the oxygen vacancy concentration is observed as a large pseudo-capacitance in the low-frequency range of AC impedance measurements [51,64]. In conventional Ni–YSZ cermet anodes, electrochemical reactions occur at the triple phase boundaries of the electronic conductor, ionic conductor, and gas because Ni is a pure electronic conductor and YSZ is a pure ionic conductor. In the case of mixed conducting ceramic electrodes, the reaction zone extends to the two phase boundaries of the electrode and gas because electrode reactions can occur via the chemical diffusion of electrons and oxygen ions through the mixed conducting oxide electrode. In such a case, the oxygen chemical potential in the electrode varies with the electric potential, which induces changes in the oxygen vacancy concentration. Therefore, the chemical capacitance observed in LSCM–GDC anodes indicates that the electrode surface is active for electrochemical reactions, and hydrogen oxidation takes place over two phase boundaries rather than three phase boundaries [65]. As shown in Fig. 6(b), a low-frequency arc was observed at a peak frequency of 0.5 Hz with a capacitance value of ~0.08 F cm^{-2}. Because both LSCM and GDC may have possibly contributed to the chemical capacitance in this composite anode, the individual chemical capacitance values for LSCM and GDC were estimated. The chemical capacitance, C_δ, can be expressed as [65];

$$C_\delta = \frac{dQ_{Chem}}{dE_{Nernst}} = \frac{d\int(2F\delta/V_m)dV}{(RT/2F)d\ln a_O} = -\frac{4F^2}{RTV_m}\frac{d\int\delta dV}{d\ln a_O} \quad (1)$$

where Q_{chem} is the charge accumulated by the chemical species, E_{Nernst} the Nernst potential associated with the oxygen chemical potential, F the Faraday constant, δ the oxygen vacancy concentration, V_m the molar volume, R the gas constant, T the temperature, and a_O the activity of oxygen. The chemical capacitance depends on the distribution of oxygen vacancies in the electrode layer [65]. Assuming that the chemical potential of oxygen changes uniformly throughout the electrode upon the application of an external potential and the entire electrode volume contributes to the chemical capacitance, the chemical capacitances of LSCM and GDC are estimated to be ~0.01 F cm^{-2} and ~1 F cm^{-2}, respectively, based on equation (1) and using the oxygen nonstoichiometry data from ref. [66–70]. These values are consistent with the chemical capacitances reported for similar materials in the literature [65], and the large difference in chemical capacitance values between LSCM and GDC can be explained by the different oxygen nonstoichiometry observed in a reducing environment. Because the capacitance of the LSCM–GDC anode obtained from the equivalent circuit fitting is ~0.08 F cm^{-2}, the chemical capacitance of the composite anode is considered to be dominated by the LSCM (50 wt%), although the contribution of the GDC (50 wt%) may not be negligible.

The impedance spectra of the Ni–YSZ anode measured at 800 °C in a humidified hydrogen (97% H_2 + 3% H_2O) atmosphere is shown in Fig. 7. The corresponding Nyquist plot (Fig. 7(a)) shows that the overall polarization resistance of the Ni–YSZ anode is slightly lower

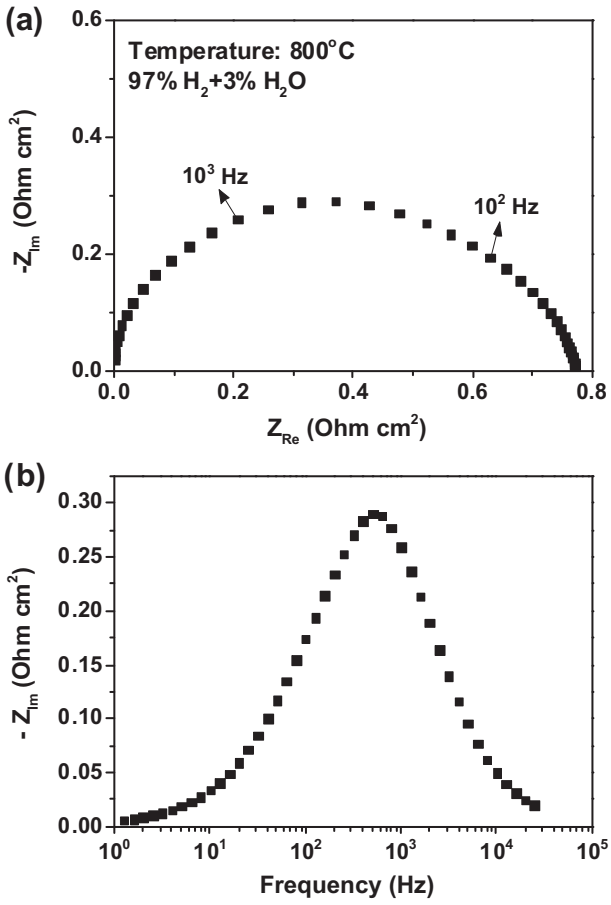

Fig. 7. Impedance spectrum of the Ni–YSZ half cell measured at 800 °C in humidified hydrogen (97% H_2 + 3% H_2O); (a) Nyquist plot and (b) Bode plot of the imaginary part.

than that of LSCM–GDC anode, which agrees with the full cell results shown in Fig. 5. The Bode plot (Fig. 7(b)) shows that the impedance spectrum of the Ni–YSZ anode is dominated by the electrode process, with a characteristic frequency of 10^2–10^3 Hz. A chemical capacitance was not observed for Ni–YSZ because the vacancy concentration of YSZ is fixed by the amount of yttria doping based on charge compensation and does not vary with the applied potential. The characteristic frequency of the impedance arc for Ni–YSZ (10^2–10^3 Hz) was somewhat higher than that of the mid-frequency arc for LSCM–GDC (10–10^2 Hz). As previously mentioned, the electrode processes within this frequency range could be related to gas–solid interactions (adsorption, dissociation, desorption, etc.) or the surface diffusion of the adsorbed species [43,44,58,59]. Because the electrochemical reactions occur at the triple phase boundaries for Ni–YSZ and at the two phase boundaries for LSCM–GDC, the major arc of Ni–YSZ is suggested to be related to the chemical process occurring at the triple phase boundaries, whereas the mid-frequency arc of LSCM–GDC is associated with gas–solid interactions. Further study is needed to specify the elementary processes that occur at the electrodes.

Additionally, the half-cell of the LSCF–GDC cathode was tested for the complete characterization of the full cells. Fig. 8(a) shows the impedance spectra of the LSCF–GDC half-cell in the form of a Nyquist plot measured at 750–850 °C in air. The polarization resistance decreases with increasing temperature, indicating thermally activated behavior for the oxygen reduction reaction. The impedance spectra of the LSCF-based cathode could also be composed of several overlapping arcs, which could be associated with gas phase diffusion,

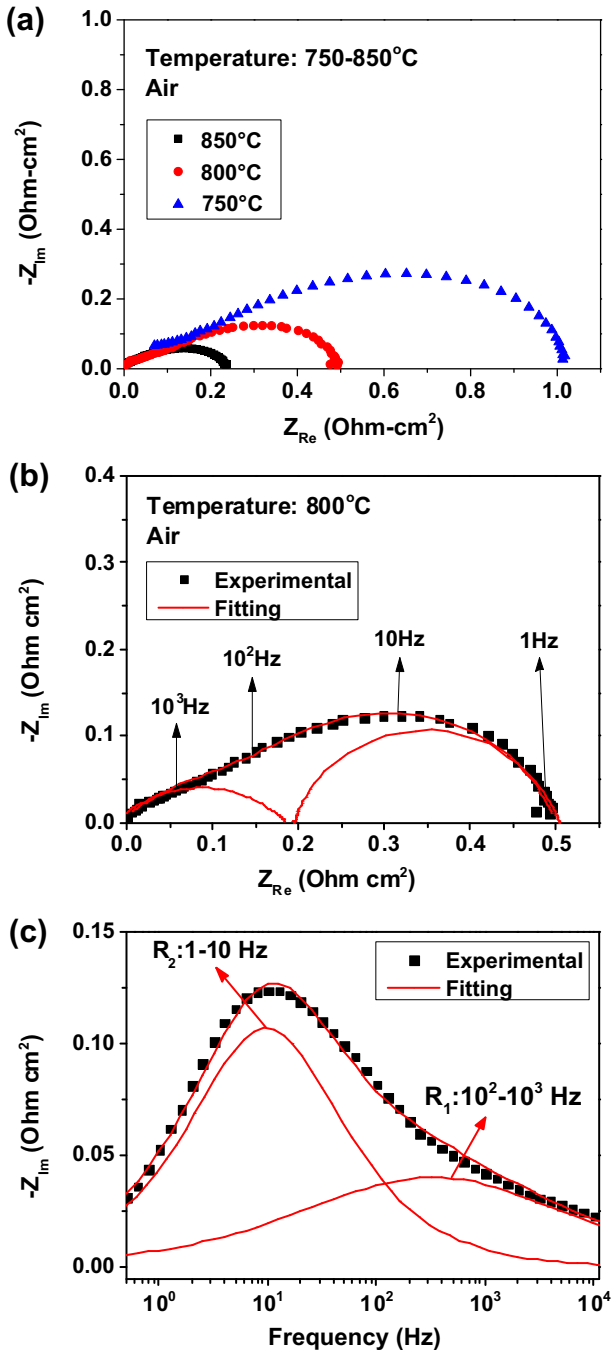

Fig. 8. Impedance spectrum of the LSCF–GDC half cell measured in air; (a) Nyquist plot between 750 and 850 °C, (b) Nyquist plot at 800 °C with fitting results, and (c) Bode plot of the imaginary part at 800 °C with fitting results.

dissociative adsorption, surface diffusion, surface exchange, charge transfer, bulk chemical diffusion, ion transfer at the electrode/electrolyte interface, etc. [71–73]. The impedance spectra were fitted well to an equivalent circuit model containing two standard resistor-constant-phase elements (R_1-CPE_1 and R_2-CPE_2), indicating that the cathode reaction is dominated by two governing processes (Fig. 8(b)). The Bode plot of the fitting results shown in Fig. 8(c) indicates that the summit frequencies for the dominant arcs are 10^2–10^3 Hz and 1–10 Hz. To identify these processes, the effect of oxygen partial pressure on the impedance characteristics was investigated and illustrated in the form of a Bode plot, as shown in Fig. 9. As shown, the

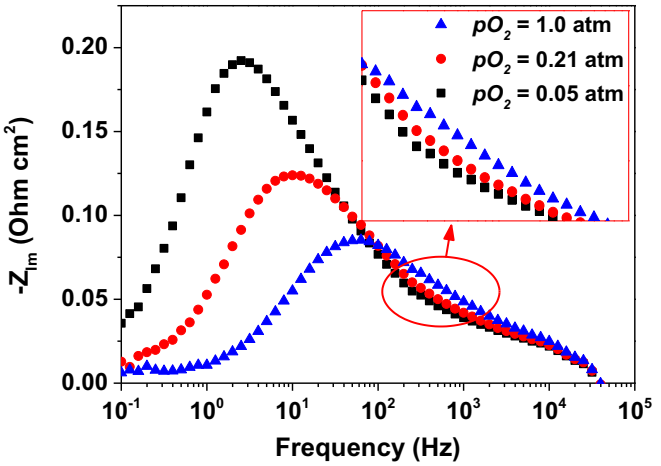

Fig. 9. Bode plot of the imaginary part of the LSCF–GDC half cell measured at 800 °C under the pO_2 range of 0.05–1.0 atm.

overall polarization resistance decreases with increasing oxygen partial pressure due to the increased oxygen concentration on the surface of the electrode. However, the high-frequency process (10^2–10^3 Hz) exhibits the opposite pO_2 dependence; the polarization resistance slightly increases with increasing oxygen partial pressure as shown in the insert of Fig. 9. The high-frequency arc of the LSCF electrode, which shows a positive dependence on pO_2, can be related to the ionic diffusion of oxygen [74,75]. The oxygen vacancy concentration in the mixed conducting electrode increases with decreasing pO_2, and the bulk diffusion resistance varies inversely with the concentration of oxygen vacancies because oxygen ions move by a vacancy mechanism [71,76]. The activation energy of the high-frequency resistance obtained from the Arrhenius plot between 700 and 850 °C is 1.7 eV, which agrees reasonably well with the activation energy for oxygen self-diffusion in $La_{0.6}Sr_{0.4}Co_{0.2}Fe_{0.8}O_{3-\delta}$ (1.9 eV) obtained by the isotopic exchange diffusion profile technique [77,78].

To identify the low-frequency process (1–10 Hz), the resistance values were plotted as a function of pO_2 in Fig. 10. The m-value in the power law describing the resistance-pO_2 relation is commonly used to determine the physical origin of the electrode process because it provides information about the type of species involved in the electrode reaction:

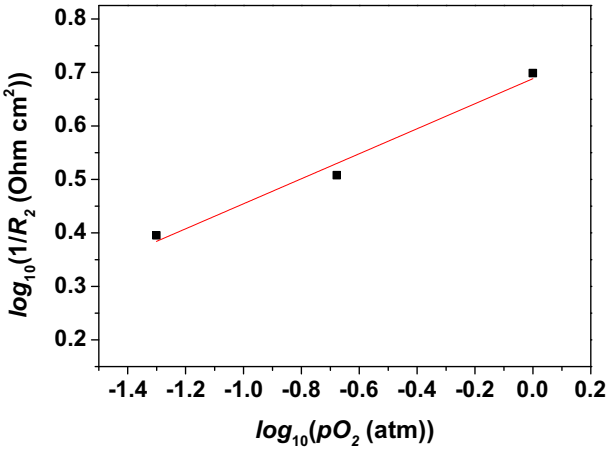

Fig. 10. Polarization resistance of the low-frequency arc of LSCF–GDC half cell measured at 800 °C as a function of pO_2.

$$R = R^o \times (pO_2)^{-m} \quad (2)$$

The pO_2 dependence illustrated in Fig. 10 fits equation (2) well, with $m = 0.24$, and the $pO_2^{-1/4}$ dependence suggests that this process is associated with adsorption and surface exchange involving atomic oxygen [79,80]. When oxygen is supplied through adsorbed adatoms on the electrode surface for the electrochemical reaction and the adatoms obey the Langmuir isotherm, the electrode resistance varies with the fourth root of pO_2. Such pO_2 dependence is usually observed in perovskite electrodes at high temperatures, where the fraction of adsorption sites occupied by oxygen atoms is substantially lower than the fraction of unoccupied sites [81]. To summarize, the reaction rate of the LSCF–GDC cathode is suggested to be governed by surface chemical exchange and solid-state oxygen diffusion, which agrees well with the previous results reported for mixed conducting perovskite air electrodes [71,82].

Based on the information collected from the half-cell measurements, the impedance spectra of the full cell in Fig. 5 can be interpreted. The impedance spectra of the all-ceramic cell with an LSCM–GDC anode and LSCF–GDC cathode show a major low-frequency peak below 1 Hz due to the chemical capacitance of LSCM–GDC. Over the frequency range of $1 \sim 10^3$ Hz, the semicircles associated with the gas–solid interaction of LSCM–GDC, surface chemical exchange of LSCF–GDC, and solid-state oxygen diffusion of LSCF overlap and show a broad spectrum. In contrast, the electrolyte-supported cell with a Ni–YSZ anode and LSCF–GDC cathode clearly shows two arcs with characteristic frequencies of 10^2–10^3 and 1–10 Hz. Because the oxygen nonstoichiometry of YSZ does not vary with the applied potential, the chemical capacitance was not observed in the low-frequency range. The larger peak at 10^2–10^3 Hz arises from the combination of the reaction at the triple phase boundary of the Ni–YSZ anode and solid-state oxygen diffusion at the LSCF cathode. The smaller impedance observed at 1–10 Hz could be attributed to the surface chemical exchange of LSCF–GDC.

4. Conclusion

All-ceramic SOFCs composed of an LSCM–GDC anode, YSZ electrolyte, and LSCF–GDC cathode are fabricated, and their electrochemical performance is evaluated. The extremely fine and homogeneous ceramic composite anode fabricated by the particle-dispersed glycine-nitrate process exhibits excellent electrochemical performance comparable to that of conventional Ni-based anodes. The impedance spectra of the full cell are successfully interpreted by the independent characterization of the cathode and anode via half-cell measurements. The impedance spectra of the LSCF–GDC cathode show two arcs related to solid-state oxide ion diffusion and surface chemical exchange. In the LSCM–GDC anode, electrochemical reactions occur over the electrode surface rather than at triple phase boundaries, and impedance associated with gas–electrode interactions is observed. The chemical capacitance resulting from the variation in the oxygen nonstoichiometry of the ceramic anode induces a major impedance arc in the low-frequency range for the LSCM–GDC anode, which should be minimized by engineering the defect chemistry of the mixed conducting electrode to improve the performance of the all-ceramic SOFC. However, to the best of the authors' knowledge, it has not been clarified how the chemical capacitance affects the power generation characteristics in SOFC operation. During the operation of SOFCs under a constant electric load, a steady state can be reached and the change in the oxygen nonstoichiometry can be minimized from a macroscopic point of view. However, from a microscopic view, local variations in the oxygen vacancy concentration accompanied due to electrochemical reactions could result in a cell resistance that is associated with the chemical capacitance and could affect the power generation efficiency. Our future work will involve an investigation of the role of the chemical capacitance in the power generation process of all-ceramic SOFCs.

Acknowledgment

This work was funded by the institutional research program of the Korea Institute of Science and Technology (2E24042), and support of Manpower Development Program for Energy of the Ministry of Knowledge and Economy (MKE), Republic of Korea, is gratefully acknowledged.

References

[1] N.Q. Minh, Journal of the American Ceramic Society 76 (1993) 563–588.
[2] P. Singh, N.Q. Minh, International Journal of Applied Ceramic Technology 1 (2004) 5–15.
[3] N.Q. Minh, Solid State Ionics 174 (2004) 271–277.
[4] S.C. Singhal, Solid State Ionics 135 (2000) 305–313.
[5] S.C. Singhal, Solid State Ionics 152 (2002) 405–410.
[6] Y.-H. Huang, R.I. Dass, Z.-L. Xing, J.B. Goodenough, Science 312 (2006) 254–257.
[7] O.A. Marina, N.L. Canfield, J.W. Stevenson, Solid State Ionics 149 (2002) 21–28.
[8] J. Liu, B.D. Madsen, Z. Ji, S.A. Barnett, Electrochemical and Solid-State Letters 5 (2002) A122–A124.
[9] S. Tao, J.T.S. Irvine, Nature Materials 2 (2003) 320–323.
[10] J. Laurencin, G. Delette, O. Sicardy, S. Rosini, F. Lefebvre-Joud, Journal of Power Sources 195 (2010) 2747–2753.
[11] B. Iwanschitz, J. Sfeir, A. Mai, M. Schutze, Journal of The Electrochemical Society 157 (2010) B269.
[12] D. Sarantaridis, A. Atkinson, Fuel Cells 7 (2007) 246–258.
[13] M. Pihlatie, A. Kaiser, M. Mogensen, Solid State Ionics 180 (2009) 1100–1112.
[14] T. Klemenso, C.C. Appel, M. Mogensen, Electrochemical and Solid-State Letters 9 (2006) A403–A407.
[15] D. Waldbillig, A. Wood, D.G. Ivey, Journal of The Electrochemical Society 154 (2007) B133–B138.
[16] D. Sarantaridis, R.J. Chater, A. Atkinson, Journal of The Electrochemical Society 155 (2008) B467–B472.
[17] Y.M. Choi, C. Compson, M.C. Lin, M. Liu, Journal of Alloys and Compounds 427 (2007) 25–29.
[18] L. Aguilar, S. Zha, Z. Cheng, J. Winnick, M. Liu, Journal of Power Sources 135 (2004) 17–24.
[19] Z. Cheng, M. Liu, Solid State Ionics 178 (2007) 925–935.
[20] Z. Cheng, S. Zha, M. Liu, Journal of Power Sources 172 (2007) 688–693.
[21] Y.M. Choi, C. Compson, M.C. Lin, M. Liu, Chemical Physics Letters 421 (2006) 179–183.
[22] A.I. Marquez, Y.D. Abreu, G.G. Botte, Electrochemical and Solid-State Letters 9 (2006) A163–A166.
[23] Y. Matsuzaki, I. Yasuda, Solid State Ionics 132 (2000) 261–269.
[24] S. Zha, Z. Cheng, M. Liu, Journal of The Electrochemical Society 154 (2007) B201–B206.
[25] B.C.H. Steele, P.H. Middleton, R.A. Rudkin, Solid State Ionics 40-41 (1990) 388–393.
[26] S. Tao, J.T.S. Irvine, The Chemical Record 4 (2004) 83–95.
[27] S. Primdahl, M. Mogensen, Solid State Ionics 152-153 (2002) 597–608.
[28] M. Mogensen, S. Primdahl, M.J. JØrgensen, C. Bagger, Journal of Electroceramics 5 (2000) 141–152.
[29] L.A. Chick, L.R. Pederson, G.D. Maupin, J.L. Bates, L.E. Thomas, G.J. Exarhos, Materials Letters 10 (1990) 6–12.
[30] S.B. Boskovic, B.Z. Matovic, M.D. Vlajic, V.D. Kristic, Ceramic Interfaces 33 (2007) 89–93.
[31] S. Park, D.W. Lee, J.C. Lee, J.H. Lee, Journal of the American Ceramic Society 86 (2003) 1508–1512.
[32] K.J. Yoon, C.A. Coyle, O.A. Marina, Electrochemistry Communications 13 (2011) 1400–1403.
[33] H. Uchida, S.-i. Arisaka, M. Watanabe, Electrochemical and Solid-State Letters 2 (1999) 428–430.
[34] A. Tsoga, A. Gupta, A. Naoumidis, P. Nikolopoulos, Acta Materialia 48 (2000) 4709–4714.
[35] S.P. Simner, J.P. Shelton, M.D. Anderson, J.W. Stevenson, Solid State Ionics 161 (2003) 11–18.
[36] J.E. Bauerle, Journal of Physics and Chemistry of Solids 30 (1969) 2657–2670.
[37] S.M. Plint, P.A. Connor, S. Tao, J.T.S. Irvine, Solid State Ionics 177 (2006) 2005–2008.
[38] P.A. Ahn, E.C. Shin, J.M. Jo, J.H. Yu, S.K. Woo, J.S. Lee, Fuel Cells 12 (2012) 1070–1084.
[39] M. Nagata, Y. Itoh, H. Iwahara, Solid State Ionics 67 (1994) 215–224.
[40] J. Rutman, I. Riess, Solid State Ionics 179 (2008) 913–918.

[41] S.B. Adler, Journal of The Electrochemical Society 149 (2002) E166–E172.
[42] B.A. Boukamp, Solid State Ionics 20 (1986) 31–44.
[43] S. Primdahl, M. Mogensen, Journal of The Electrochemical Society 144 (1997) 3409–3419.
[44] S.P. Jiang, S.P.S. Badwal, Solid State Ionics 123 (1999) 209–224.
[45] M. Ihara, T. Kusano, C. Yokoyama, Journal of The Electrochemical Society 148 (2001) A209–A219.
[46] S. Raz, K. Sasaki, J. Maier, I. Riess, Solid State Ionics 143 (2001) 181–204.
[47] J. Mizusaki, H. Tagawa, Y. Miyaki, S. Yamauchi, K. Fueki, I. Koshiro, K. Hirano, Solid State Ionics 53–56 (1) (1992) 126–134.
[48] S.P. Jiang, S.P.S. Badwal, Journal of The Electrochemical Society 144 (1997) 3777–3784.
[49] S. Primdahl, M. Mogensen, Journal of The Electrochemical Society 146 (1999) 2827–2833.
[50] S. Primdahl, M. Mogensen, Journal of The Electrochemical Society 145 (1998) 2431–2438.
[51] J. Jamnik, J. Maier, Physical Chemistry Chemical Physics 3 (2001) 1668–1678.
[52] W.G. Bessler, J. Warnatz, D.G. Goodwin, Solid State Ionics 177 (2007) 3371–3383.
[53] B. Bhatia, D.S. Sholl, The Journal of Chemical Physics 122 (2005) 204707–204708.
[54] Y.R. Dar, P. Vijay, M.O. Tadé, R. Datta, Journal of Electroanalytical Chemistry 677–680 (2012) 15–23.
[55] K. Eguchi, Y. Kunisa, K. Adachi, M. Kayano, K. Sekizawa, H. Arai, Chemistry Letters 24 (1995) 963–964.
[56] S. Gewies, W.G. Bessler, V. Sonn, E. Ivers-Tiffee, ECS Transactions 7 (2007) 1573–1582.
[57] P. Holtappels, I.C. Vinke, L.G.J. de Haart, U. Stimming, Journal of The Electrochemical Society 146 (1999) 2976–2982.
[58] J. Mizusaki, H. Tagawa, T. Saito, T. Yamamura, K. Kamitani, K. Hirano, S. Ehara, T. Takagi, T. Hikita, M. Ippommatsu, S. Nakagawa, K. Hashimoto, Solid State Ionics 70–71 (1) (1994) 52–58.
[59] C. Jin, C. Yang, F. Chen, Journal of The Electrochemical Society 158 (2011) B1217–B1223.
[60] M.D. Gross, J.M. Vohs, R.J. Gorte, Electrochemical and Solid-State Letters 10 (2007) B65–B69.
[61] M. van den Bossche, R. Matthews, A. Lichtenberger, S. McIntosh, Journal of The Electrochemical Society 157 (2010) B392–B399.
[62] T. Delahaye, T. Jardiel, O. Joubert, R. Laucournet, G. Gauthier, M.T. Caldes, Solid State Ionics 184 (2011) 39–41.
[63] R. Barfod, M. Mogensen, T. Klemensø, A. Hagen, Y.-L. Liu, P. Vang Hendriksen, Journal of The Electrochemical Society 154 (2007) B371–B378.
[64] T. Kawada, J. Suzuki, M. Sase, A. Kaimai, K. Yashiro, Y. Nigara, J. Mizusaki, K. Kawamura, H. Yugami, Journal of The Electrochemical Society 149 (2002) E252–E259.
[65] T. Nakamura, T. Kobayashi, K. Yashiro, A. Kaimai, T. Otake, K. Sato, J. Mizusaki, T. Kawada, Journal of The Electrochemical Society 155 (2008) B563–B569.
[66] K. Yashiro, T. Suzuki, A. Kaimai, H. Matsumoto, Y. Nigara, T. Kawada, J. Mizusaki, J. Sfeir, J. Van herle, Solid State Ionics 175 (2004) 341–344.
[67] K. Yashiro, S. Onuma, A. Kaimai, Y. Nigara, T. Kawada, J. Mizusaki, K. Kawamura, T. Horita, H. Yokokawa, Solid State Ionics 152–153 (2002) 469–476.
[68] S. Wang, H. Inaba, H. Tagawa, M. Dokiya, T. Hashimoto, Solid State Ionics 107 (1998) 73–79.
[69] J. Mizusaki, M. Hasegawa, K. Yashiro, H. Matsumoto, T. Kawada, Solid State Ionics 177 (2006) 1925–1928.
[70] M. Oishi, K. Yashiro, K. Sato, J. Mizusaki, T. Kawada, Journal of Solid State Chemistry 181 (2008) 3177–3184.
[71] S.B. Adler, J.A. Lane, B.C.H. Steele, Journal of The Electrochemical Society 143 (1996) 3554–3564.
[72] D.Z. de Florio, R. Muccillo, V. Esposito, E. Di Bartolomeo, E. Traversa, Journal of The Electrochemical Society 152 (2005) A88–A92.
[73] N. Grunbaum, L. Dessemond, J. Fouletier, F. Prado, A. Caneiro, Solid State Ionics 177 (2006) 907–913.
[74] A. Esquirol, N.P. Brandon, J.A. Kilner, M. Mogensen, Journal of The Electrochemical Society 151 (2004) A1847–A1855.
[75] G. DiGiuseppe, L. Sun, Int. J. Hydrogen Energy 36 (2011) 5076–5087.
[76] Y.-M. Kim, S.-I. Pyun, J.-S. Kim, G.-J. Lee, Journal of The Electrochemical Society 154 (2007) B802–B809.
[77] B.C.H. Steele, J.-M. Bae, Solid State Ionics 106 (1998) 255–261.
[78] R.J. Chater, S. Carter, J.A. Kilner, B.C.H. Steele, Solid State Ionics 53–56 (2) (1992) 859–867.
[79] A. Ringuedé, J. Fouletier, Solid State Ionics 139 (2001) 167–177.
[80] Y. Takeda, R. Kanno, M. Noda, Y. Tomida, O. Yamamoto, Journal of The Electrochemical Society 134 (1987) 2656–2661.
[81] D.Y. Wang, A.S. Nowick, Journal of The Electrochemical Society 126 (1979) 1155–1165.
[82] S.B. Adler, Solid State Ionics 111 (1998) 125–134.